ELSEVIER

Efficient orientational averaging by the extension of Lebedev grids via regularized octahedral symmetry expansion

Baltzar Stevensson *, Mattias Edén *

Physical Chemistry Division, Arrhenius Laboratory, Stockholm University, SE-106 91 Stockholm, Sweden

Abstract

Gaussian spherical quadrature methods in the guise of the Lebedev sampling grids are highly efficient for some orientational ("powder") averaging problems in solid state NMR. However, their applicability is currently restricted, as the sets of orientations are derived analytically and because they are not well adapted to simulate the broad peakshapes encountered, for example, in the NMR on static powders or on half-integer quadrupolar spins subject to second order quadrupolar interactions under magic-angle spinning conditions. We remedy these problems by (i) introducing the recursive procedure *regularized octahedral symmetry expansion* (ROSE), to which any existing Lebedev set may be subjected. Each recursive step gives a 9-fold enlarged set of orientations. (ii) We demonstrate that ROSE-expanded grids, in conjunction with spectral interpolation, is well suited for calculating broad peakshapes. These advances combine into the apparently most efficient general-purpose two-angle orientational averaging technique proposed to date for solid state NMR applications.

© 2006 Elsevier Inc. All rights reserved.

Keywords: Magic-angle-spinning NMR; Powder average; Regularization; Orientational symmetry; Gaussian spherical quadrature; Quadrupolar spins; Interpolation; Numerical integration

1. Introduction

The concept of *numerical integration* enters in many branches of Chemical Physics: for example, essentially all solid state NMR experiments are nowadays carried out on powders comprising a vast number of randomly oriented micro-crystallites. In the analysis of experimental data, it is crucial to be able to numerically calculate the NMR response. It depends for each crystallite on the relative orientation (Ω) between the spin interaction tensor and the external magnetic field direction [1–18]. The net NMR time signal of the powder, denoted $\langle s(t;\Omega)\rangle_{\Omega} \equiv \bar{s}(t)$, is calculated as the average over all crystallite orientations Ω: the procedure is usually termed "powder averaging" and is equivalent to an *integration* over Ω.

However, as the integration may in general not be performed analytically, the *orientational* (powder) *averaging* is traditionally carried out by sampling a set of N^S crystallite orientations $\{\Omega_j^S\}$ and approximating the orientational average as follows:

$$\bar{s}(t) \approx \bar{s}^S(t), \tag{1}$$

where the *estimated* average is calculated as a weighted sum over the signals from all sampled orientations,

$$\bar{s}^S(t) = \sum_{j=1}^{N^S} w_j^S s(t; \Omega_j^S) \tag{2}$$

with the weights w_j^S normalized according to

$$\sum_{j=1}^{N^S} w_j^S = 1. \tag{3}$$

Unfortunately, as the powdered sample typically comprises 10^7–10^8 crystallites and the calculation involving *each*

* Corresponding authors. Fax: +46 8 152 187 (M. Edén).
  E-mail addresses: baltzar.stevensson@physc.su.se (B. Stevensson), mattias@physc.su.se (M. Edén).

crystallite is often time consuming, it is desirable to minimize N^S by a careful choice of the selected orientations $\{\Omega_j^S\}$, while achieving the most accurate approximation in Eq. (1). A large number of orientational sampling schemes have been proposed for solving this task, most of which aim at generating the most *uniform* distribution of orientations [1–7,19–21]. So far, the most popular approaches employed in solid state NMR apply this concept: here we single out the ZCW technique of Zaremba, Conroy, Wolfsberg and co-workers [19–21], the method by Alderman, Solum and Grant (ASG) [1], and the REPULSION scheme by Bak and Nielsen [7]. We refer to the literature for detailed accounts of these methods.

A powerful integration technique, employed for instance extensively in DFT calculations [22–27], is Gaussian spherical quadrature (GSQ) [24,28–34], of which the most efficient sampling schemes (henceforth labeled "LEB"), are those of Lebedev and co-workers [28–33]. Ref. [10] demonstrated that the Lebedev schemes have decisive advantages over other orientational averaging techniques for calculations of spinning sideband manifolds generated from commuting spin interactions [35], such as chemical shift anisotropies, first-order quadrupolar interactions and heteronuclear dipolar-couplings [16,35]. As reviewed in Refs. [10,11,15,18] only two orientational variables enter explicitly the numerical integration in these cases, and the structurally related information (coupling constants, asymmetry parameters) is encoded in the width and shape of the sideband manifold and accessible through numerical iterative fitting incorporating orientational averaging. In general, the larger the number of spinning sidebands present in the spectrum, the larger the number of sampled orientations required to obtain sufficiently accurate sideband amplitudes. The Lebedev schemes may often provide a set of *exact* amplitudes using less than 100 sampled orientations, thereby outperforming any other orientational averaging method proposed to date [10]. This is partly because they are well-adapted to handle the orientational symmetry of many NMR problems [10,11,15,18].

However, the Lebedev schemes have primarily two shortcomings: first, the sets of orientations are derived analytically, and despite that expanded sets are continuously being presented [28–33], there are still classes of very challenging problems, such as the calculation of satellite-transition sideband manifolds of half-integer quadrupolar nuclei subject to MAS [36], for which the largest existing Lebedev sets are insufficient.

The Lebedev schemes have also a deficiency in that they are not well adapted to simulate *broad* peakshapes [10], for instance those obtained from static powders or from second-order-broadened central-transition lineshapes of quadrupolar spins undergoing MAS [16,36]. Here, a fundamental problem is the incompatibility of representing lineshapes spanning large frequency-ranges by using a *small* set of calculated frequencies and amplitudes. This problem is shared by all orientational sampling schemes. However, it may be remedied, thereby leading to significantly reduced computational times, by using spectral *interpolation* techniques, of which that of Alderman, Solum, and Grant in conjunction with their orientational sampling scheme has found most widespread use in solid state NMR [1]. An extension of the interpolation procedure to simulations of 2D experiments was given in Ref. [9], and other methods based on interpolation concepts have also been proposed [2,5,37].

In this contribution, we remedy the two shortcomings of the Lebedev schemes as follows: (i) we introduce a straightforward expansion protocol, termed *regularized octahedral symmetry expansion* (ROSE), to which any existing Lebedev set may be subjected. The outcome is an enlarged set of orientations (by about a factor of 9) denoted ^{ROSE}LEB. It retains the symmetry of the input set and closely *approximates* the not yet existing "ideal" Lebedev version. The new grids are well-adapted to handle very challenging NMR simulations involving hundreds of spinning sidebands. (ii) We demonstrate that both the LEB and ^{ROSE}LEB schemes are straightforward to incorporate into the ASG interpolation protocol [1], thereby greatly extending their application areas. Further, we show that the ^{ROSE}LEB schemes in conjunction with ASG interpolation provide slightly more accurate results than using the original ASG orientations of Ref. [1].

The remainder of this article is organized as follows: the next section introduces the basics of orientational averaging, including the principles of GSQ and a brief review of orientational symmetry in NMR [10,11,15,18]. The third section introduces the ROSE protocol, which in the subsequent section is compared with existing state-of-the-art orientational averaging methods for the calculation of spinning sideband manifolds generated by a single spin-3/2 subject to a MAS-modulated first order quadrupolar interaction. Section 5 evaluates the performance of the new interpolated sampling schemes in the context of simulating central-transition lineshapes of a spin-3/2 broadened by second order quadrupolar interactions. Our numerical procedures are discussed in Section 6, and the last section concludes.

2. Principles of orientational averaging

2.1. Orientational dependence of the NMR signal

The Hamiltonian of an anisotropic spin interaction Λ may generally be expressed as a product of an orientation dependent frequency $\omega_\Lambda(\Omega)$ and a spin operator $\widehat{T}_\Lambda$:

$$\widehat{H}_\Lambda = \omega_\Lambda(\Omega)\widehat{T}_\Lambda. \tag{4}$$

In a sample comprising randomly oriented crystallites and undergoing rotation around an axis subtending the "magic angle" $\theta_m = \arctan\{\sqrt{2}\}$ with respect to the external magnetic field direction, the frequency is both *orientation* and *time*-dependent. For a single crystallite of the powder, it may be expressed [15,16,18,38–42]:

$$\omega_\Lambda(t;\Omega_{MR}) = \sum_{q=-2}^{2} \sum_{q',q''=-2}^{2} [A_{2q''}]^P D_{q''q'}^2(\Omega_{PM}) D_{q'q}^2(\Omega_{MR}) d_{q0}^2(\theta_m)$$
$$\times \exp\{iq\omega_r t\}, \tag{5}$$

where ω_r is the spinning frequency and $D_{qq'}^2(\Omega)$ and $d_{qq'}^2(\beta)$ denote second rank Wigner functions and reduced Wigner functions, respectively. They are related by

$$D_{qq'}^J(\alpha,\beta,\gamma) = \exp\{-i(\alpha q + \gamma q')\} d_{qq'}^J(\beta) \tag{6}$$

for an arbitrary rank J [43]. Here we assumed that the spin interaction Λ is second rank with respect to rotations in space and may consequently be expressed in its principal axis system (PAS) as a set of five components $[A_{2q}]^P$, where q takes integer values in the range $-2 \leqslant q \leqslant 2$ [15,16,18,38–42,44]. The laboratory-frame frequency $\omega_\Lambda(t;\Omega_{MR})$ is calculated according to Eq. (5) as a series of rotations, where each individual transformation between two coordinate systems F and F$'$ is parametrized by an Euler angle triplet $\Omega_{FF'} = \{\alpha_{FF'}, \beta_{FF'}, \gamma_{FF'}\}$ [43]. The transformations involve sequentially (i) the "molecular frame" (M), representing an arbitrary coordinate system fixed at a crystal fragment, (ii) a "rotor frame" (R) fixed on the sample holder and (iii) the laboratory frame (L). Here the angles $\Omega_{RL} = \{-\omega_r t, \theta_m, 0\}$ are time-dependent, while the spatial orientational dependence of a given crystallite is encoded in $\Omega_{MR} = \{\alpha_{MR}, \beta_{MR}, \gamma_{MR}\}$. Over the powder of randomly oriented crystallites, Ω_{MR} spans the entire range of values $\{0 \leqslant \alpha_{MR} < 2\pi, 0 \leqslant \beta_{MR} \leqslant \pi, 0 \leqslant \gamma_{MR} < 2\pi\}$.

In the general case, the Hamiltonian is a sum over several interactions Λ_j, each being associated with a certain set of angles Ω_{PM}^j. However, if one is dealing with a *single* interaction and identifies its PAS with the molecular frame, Eq. (5) may be written

$$\omega_\Lambda(t;\Omega_{PR}) = \sum_{q=-2}^{2} \sum_{q'=-2}^{2} [A_{2q'}]^P D_{q'q}^2(\Omega_{PR}) d_{q0}^2(\theta_m) \exp\{iq\omega_r t\}. \tag{7}$$

In this case, the orientational dependence is encoded in Ω_{PR}. In the following, we use the shorthand notation $\Omega \equiv \Omega_{PR}$ and $\Omega \equiv \Omega_{MR}$, when dealing with *one* interaction and *several* interactions, respectively. As explained in detail in Ref. [18], the orientational dependence of the spin Hamiltonian translates into an orientation dependent NMR time signal $s(t,\Omega)$, which upon Fourier transformation results in an NMR spectrum $S(\omega,\Omega)$. The latter is represented as a set of amplitudes a_i at corresponding frequency coordinates ω_i. In general, *both* the spectral *amplitudes* and *frequencies* depend on orientation. This is the scenario for NMR interactions in static (non-rotating) powders, spin-pairs at rotational resonance or quadrupolar spins subject to second order quadrupolar interactions both in static and rotating samples [16,36,45,46].

However, MAS spin dynamics governed by a so-called *dynamically inhomogeneous* Hamiltonian (implying that it is self-commuting at all times) [35], leads to a spectrum comprising a set of narrow "spinning sidebands," positioned at the discrete and equally spaced frequencies $\omega_j^{(k)} = \omega_j^{(0)} + k\omega_r$ [8,12,35,44,47,48]. Here $\omega_j^{(0)} = \omega_{iso}^\Lambda$ denotes the isotropic (orientation *in*dependent) part of the spatial tensor. In this case, the spectral amplitudes $a_j^{(k)}(\Omega)$ depend on orientation, while the frequencies do *not*. Examples of interactions giving dynamically inhomogeneous spin dynamics are chemical shift anisotropies, heteronuclear dipolar interactions and first order quadrupolar interactions [35]. In practice, the width of a spinning sideband is only limited by spin–spin relaxation (T_2). However, in the following, we ignore relaxation effects and treat each sideband as an infinitely narrow "stick" with amplitude $a_j^{(k)}(\Omega)$ and frequency $\omega_j^{(k)} = k\omega_r$, i.e., we further assume that $\omega_{iso}^\Lambda = 0$.

2.2. The orientational average

The calculation of the NMR time-domain signal or frequency-domain spectrum from a powder of randomly oriented crystallites may be performed by integrating the orientational variable over its full range of definition, $V^{(3)} = \{0 \leqslant \alpha < 2\pi, 0 \leqslant \beta \leqslant \pi, 0 \leqslant \gamma < 2\pi\}$:

$$\bar{f} = \mathcal{N}^{(3)} \int_{V^{(3)}} f(\Omega) \, d\Omega, \tag{8}$$

where $\bar{f}$ is the *orientational* (powder) *average*, and the normalization constant $\mathcal{N}^{(3)}$ is equal to the reciprocal integration volume $(8\pi^2)^{-1}$. In NMR, we identify $f(\Omega)$ with either $s(t,\Omega)$ or $S(\omega,\Omega)$.

2.3. Orientational symmetry

As discussed in detail in Refs. [8–12,15,18], for simulations of spin systems not subject to radio frequency (rf) pulses during the NMR signal acquisition and being associated with an initial density operator not depending on orientation at the start of acquisition $[\hat{\rho}(t=0)]$, the integration (average) over γ may be handled separately. Then the orientational averaging reduces to an integration over only α and β:

$$\bar{f} = \mathcal{N}^{(2)} \int_{V^{(2)}} f(\alpha,\beta) \, d\alpha \sin\beta \, d\beta \tag{9}$$

with

$$V^{(2)} = \{0 \leqslant \alpha < 2\pi, 0 \leqslant \beta \leqslant \pi\},$$
$$\mathcal{N}^{(2)} = (4\pi)^{-1}. \tag{10}$$

Note that $V^{(2)}$ represents the unit sphere surface if we identify $\{\alpha,\beta\}$ with the polar angles $\{\theta,\phi\}$ according to $\alpha \equiv \phi$ and $\beta \equiv \theta$ [43].

However, for these restricted NMR problems, the integration range [Eq. (10)] may always be reduced further due to *additional* symmetries of $f(\alpha,\beta)$. Refs. [10,11,15,18] provide thorough discussions; we simply note that in the most general case of several interactions with non-coincid-

ing principal axis systems, the relevant integration range $V^{(2)}$ is essentially corresponding to a *hemisphere*,

$$V^{(2)} = \{0 \leqslant \alpha < 2\pi, 0 \leqslant \beta < \pi/2\} \cup \{0 \leqslant \alpha < \pi, \beta = \pi/2\},$$
$$\mathcal{N}^{(2)} = (2\pi)^{-1}, \tag{11}$$

where $\cup$ represents the union symbol. In the case of a *single* interaction, $V^{(2)}$ reduces to an *octant*:

$$V^{(2)} = \{0 \leqslant \alpha \leqslant \pi/2, 0 \leqslant \beta \leqslant \pi/2\},$$
$$\mathcal{N}^{(2)} = (\pi/2)^{-1}. \tag{12}$$

Finally, in the case of a single interaction associated with an *axially symmetric* tensor, $f(\alpha, \beta)$ has no dependence on α, allowing integration over a one-dimensional spherical arc:

$$V^{(1)} = \{0 \leqslant \beta \leqslant \pi/2\},$$
$$\mathcal{N}^{(1)} = 1. \tag{13}$$

Note that a prerequisite for using Eqs. (12) and (13) is that the "molecular frame" is coincident with the PAS of the tensor, i.e., $\Omega_{PM} = \{0, 0, 0\}$. Then the relevant orientational variable is $\Omega \equiv \Omega_{PR}$ as in Eq. (7).

2.4. Gaussian spherical quadrature

2.4.1. General principles

Assume that a function $f(\Omega) = f(\alpha, \beta, \gamma)$ is expanded in a series of orthogonal Wigner functions [Eq. (6)]. Provided that the prerequisites leading to Eqs. (9) and (10) are fulfilled, $f(\Omega)$ only depends on *two* variables, $f(\Omega) = f(\alpha, \beta)$, and may consequently be expanded as

$$f(\alpha, \beta) = \sum_{J=0}^{\infty} \sum_{q=-J}^{J} f_{Jq} D_{q0}^{J}(\alpha, \beta). \tag{14}$$

An efficient, stable and accurate approach to evaluating Wigner functions for large J is outlined in Appendix A. In the most general case when $f(\alpha, \beta, \gamma)$ depends on all three Euler angles $\Omega = \{\alpha, \beta, \gamma\}$, the expansion coefficients as well as the Wigner functions have two independent indices q and q' [10]. In order to better bring out the analogy with this scenario, we employ the notation $D_{q0}^{J}(\alpha, \beta)$, but note that $D_{q0}^{J}(\alpha, \beta)$ is directly related to the spherical harmonic $Y_{Jq}(\beta, \alpha) \equiv Y_{Jq}(\theta, \phi)$ [43]. We next assume that the expansion [Eq. (14)] is convergent and generally that $|f_{J_1 q}| \gg |f_{J_2 q}|$ for $J_2 \gg J_1$, i.e., that the coefficients f_{Jq} associated with low J are dominating those of high J. Further, we assume that the series is "exact" when truncated at $J = J_{max}^f$.

The *orientational average* of $f(\alpha, \beta)$ may be expressed [10]

$$\bar{f} = \mathcal{N}^{(2)} \int_{V^{(2)}} f(\alpha, \beta) \, d\alpha \sin \beta \, d\beta \tag{15}$$

$$= \mathcal{N}^{(2)} \sum_{J=0}^{J_{max}^f} \sum_{q=-J}^{J} f_{Jq} \int_{V^{(2)}} D_{q0}^{J}(\alpha, \beta) \, d\alpha \sin \beta \, d\beta, \tag{16}$$

with $\mathcal{N}^{(2)}$ and $V^{(2)}$ given by Eqs. (10). Due to the following property of the Wigner functions [43],

$$\int_{V^{(2)}} D_{q0}^{J}(\alpha, \beta) \, d\alpha \sin \beta \, d\beta = 4\pi \delta_{J,0} \delta_{q,0} \tag{17}$$

all terms in Eq. (16) vanish, except that associated with $J = 0$. Here $\delta_{x,y}$ denotes the Kronecker delta function. Eq. (16) now reduces to [10]

$$\bar{f} = f_{00} \tag{18}$$

implying that the orientational average of $f(\alpha, \beta)$ is equal to the expansion coefficient f_{00} in Eq. (14).

The integration technique Gaussian spherical quadrature (GSQ) [24,28–34] aims at selecting orientations and weights such that the set $S = \{\alpha_j^S, \beta_j^S, w_j^S\}$ integrates all $(J_{max}^S + 1)^2$ Wigner functions $D_{q0}^{J}(\alpha, \beta)$ with $J \leqslant J_{max}^S$ exactly, where J_{max}^S is characteristic of S [10]. The integration of $f(\alpha, \beta)$ is then *exact* provided that $J_{max}^S \geqslant J_{max}^f$. Typically, a GSQ set with high J_{max}^S is significantly larger than a set with low J_{max}^S. In general, the number of orientations N^S grows linearly with J_{max}^S as well as with the number of independent integration variables, i.e., $\sim (J_{max}^S)^2$ orientations are required to integrate all $D_{q0}^{J}(\alpha, \beta)$ functions for $J \leqslant J_{max}^S$. Note that a function $f(\alpha, \beta)$ associated with a high J_{max}^f is "difficult" to integrate and requires a large set S. GSQ techniques are therefore most efficient for integrating functions with relatively low J_{max}^f, in practice $J_{max}^S \lesssim 100$. It has been demonstrated that the prerequisites for successful implementation of GSQ techniques are fulfilled for many NMR problems and further that GSQ is the *only* technique capable of providing *exact* powder averages using a *finite* set of orientations [10].

The orientational averaging grids of Lebedev and co-workers [28–33] are the most efficient GSQ schemes known to date. They have the following approximate relationship between J_{max}^S and the number of orientations:

$$N_{LEB}^S \approx \tfrac{1}{3}(J_{max}^S + 1)^2. \tag{19}$$

The so far largest reported Lebedev set is associated with $J_{max} = 131$ and comprises 5810 orientations [33].

2.4.2. Sampling moments and rank profiles

As an assessment of the orientational averaging performance of a set comprising N^S orientations and weights $\{\alpha_j^S, \beta_j^S, w_j^S\}$, it is convenient to introduce a *sampling moment* [10]

$$\sigma_{Jq}^S = \sum_{j=1}^{N^S} w_j^S D_{q0}^{J}(\alpha_j^S, \beta_j^S), \tag{20}$$

whereupon Eq. (16) is approximated according to

$$\bar{f} \approx \bar{f}^S = \sum_{J=0}^{J_{max}^f} \sum_{q=-J}^{J} f_{Jq} \sigma_{Jq}^S. \tag{21}$$

If Eq. (3) is obeyed, $\sigma_{00}^S = 1$. For simplicity, we onwards calculate the root-mean square (rms) sampling moment, defined as [10]

$$\sigma_J^S = \left((2J+1)^{-1} \sum_{q=-J}^{J} |\sigma_{Jq}^S| \right)^{\frac{1}{2}}. \qquad (22)$$

Hence, a sampling scheme arranging that $\sigma_J^S = 0$ for all J associated with finite expansion coefficients f_{Jq} in Eq. (14) gives an exact orientational average, $\bar{f}^S = \bar{f}$. Finite values of σ_{Jq}^S for $J \leqslant J_{max}^f$ introduces integration errors, but if the coefficients f_{Jq} fall off rapidly when J increases, a "good" orientational averaging scheme arranges $\sigma_J^S \approx 0$ for all $J \leqslant J_{max}^f$, and thereby a sufficiently accurate estimate of $\bar{f}$.

If the function has one of the orientational symmetries discussed in the previous section, some of the expansion coefficients f_{Jq} are zero. *Provided* that the scheme samples orientations under the given symmetry, a straightforward reduction of the grid-size is then possible. For example, if the function $f(\alpha, \beta)$ has inversion symmetry, all coefficients f_{Jq} for odd J are zero [10], which allows integration over hemispheric range defined in Eq. (11). If the sampling scheme generates orientations under inversion symmetry, N^S can be reduced by a factor of 2. As the computational time grows linearly with the number of sampled orientations, it follows that hemispheric and octant sets leads ideally to two and eight times faster calculations. This applies, for example, to both the Lebedev and ASG schemes as they are implemented under octahedral symmetry. The ZCW sets, however, *lacks* inversion symmetry; while they *may* easily be generated over a hemisphere or octant, these reduced sets do not necessarily give more accurate orientational averages than their full-sphere versions [10].

In the following, we label schemes sampled over a hemisphere or an octant by appending the letters "h" and "o," respectively, to the parent scheme label. For example, the complete Lebedev set with $J_{max} = 101$ comprises 3470 ori-

entations and is denoted LEB3470, whereas the corresponding hemispheric set is denoted LEBh1735 (comprising 1735 orientations) and the octant set is labeled LEBo460.

Fig. 1 plots rms sampling moments σ_J against J for three schemes: ZCWh, ASGh, and LEBh. Overall, σ_J decreases as the number of orientations increases, which reflects the well-known impetus for choosing a large set in order to obtain an accurate estimate of the orientational average. The rank profiles share the common feature of initially being rather flat, after which a sharp peak appears, followed by a region of overall high values of σ_J. If the function to be integrated has a J_{max}^f falling within the flat region of a given rank profile, the corresponding set of orientations provides a decent estimate of the orientational average, which improves further as the number of orientations increases.

However, only the Lebedev schemes cancel σ_J, thereby giving *exact* averages, provided that $J_{max}^S \geqslant J_{max}^f$. The rank profile of the largest hemispheric Lebedev set ($J_{max} = 131$) is shown in Fig. 1H. However, in cases for which $J_{max}^f > 131$, insufficient accuracy of the orientational average may result. As outlined in the next section, we have remedied this situation by developing a straightforward expansion protocol to which any existing Lebedev set may be subjected. The rank profile of such an expanded Lebedev set is displayed in Fig. 1I: it is denoted ^{ROSE}LEBh17497 and resulted from the input set LEBh1945, associated with $J_{max} = 107$. The rank profile of ^{ROSE}LEBh17497 peaks at the very high rank $J = 324$. This set does not cancel any sampling moment, which implies that the ROSE schemes are strictly not belonging to the GSQ category. Nevertheless, as all sampling moments below the "peak" $J < 324$ are negligible, the loss of integration accuracy is for all practical purposes insignificant, as will be demonstrated below. Also, note that for
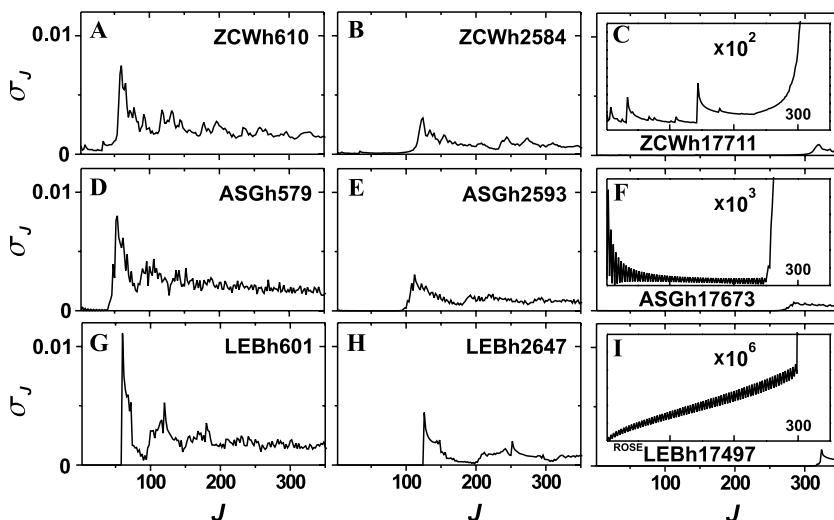

Fig. 1. Rms sampling moments σ_J plotted for even ranks J using the set of orientations indicated in each plot, for the following schemes: ZCWh (A–C), ASGh (D–F), LEBh (G and H), and ^{ROSE}LEBh (I). The rms sampling moment σ_0 is by definition equal to 1 and is not displayed. The inset plots display the rank profiles on a magnified vertical scale, by a factor of 100 (C), 1000 (F), and 10^6 (I) relative that of the other graphs. Note the more than 1000-fold reduced sampling moments (for $J \lesssim 300$) of the ^{ROSE}LEBh set relative to those of ZCWh and ASGh.

$J < 324$, the rms sampling moments of the ^{ROSE}LEBh set are several orders of magnitude smaller than the corresponding values of ASGh and ZCWh.

3. Regularized octahedral symmetry expansion

The GSQ schemes of Lebedev and co-workers are derived (semi)-*analytically* [28–33]. The problem of generating larger "Lebedev sets" has also been addressed by numerical techniques [24,34]. However, this task is challenging in terms of computational time and memory if one only relies on "brute-force" numerical methods. While being straightforward to generate, our expanded Lebedev sets ^{ROSE}LEB are constructed so as to *approximate* the *asymptotic* behavior of the exact Lebedev orientations as their number increases. There are several degrees of freedom in this procedure: *each recursive step in the ROSE protocol presented here results in a 9-fold enlargement of the input grid.*

The Lebedev sets conform to the octahedral point group with inversion G_*^8 [28–33]. We have found that all existing sets are not suitable for orientational averaging in NMR: within this group count for example some members involving negative weights w_j. In this work, we have only fed the most uniform Lebedev sets through the ROSE procedure. For such grids, all weights are positive and almost equal,

with the following relationship applying between J_{max} and N_{LEB}^S:

$$N_{LEB}^S = \tfrac{1}{3}(J_{max} + 1)^2 + 2, \quad J_{max} = \{5, 11, 17, \ldots, 131\}.$$

(23)

For these grids, $(J_{max} + 1)$ is a multiple of six [32].

The ROSE procedure produces an expanded set associated with an "effective" J_{max}^{eff}, while maintaining the original Lebedev symmetry and relationship between J_{max}^{eff} and N^S [Eq. (23)]. The notation J_{max}^{eff} implies that all sampling moments for ranks $1 \leqslant J \leqslant J_{max}^{eff}$ are negligibly *small but finite*, as opposed to those of the exact LEB sets that *cancel*. In Fig. 2A, the input set LEB50 ($J_{max} = 11$) is used to exemplify the ROSE procedure, leading to a set of orientations that closely mimics the existing LEB434 set with $J_{max} = 35$ shown in Fig. 2E. A collection of ^{ROSE}LEB sets are given in Table 1.

The remainder of this section outlines the two elements of the expansion procedure, together combining into *one* ROSE step that may be applied recursively.

3.1. Octahedral symmetry expansion

As a preparatory step, the input Lebedev orientations are connected into a "triangulated grid," where three near-
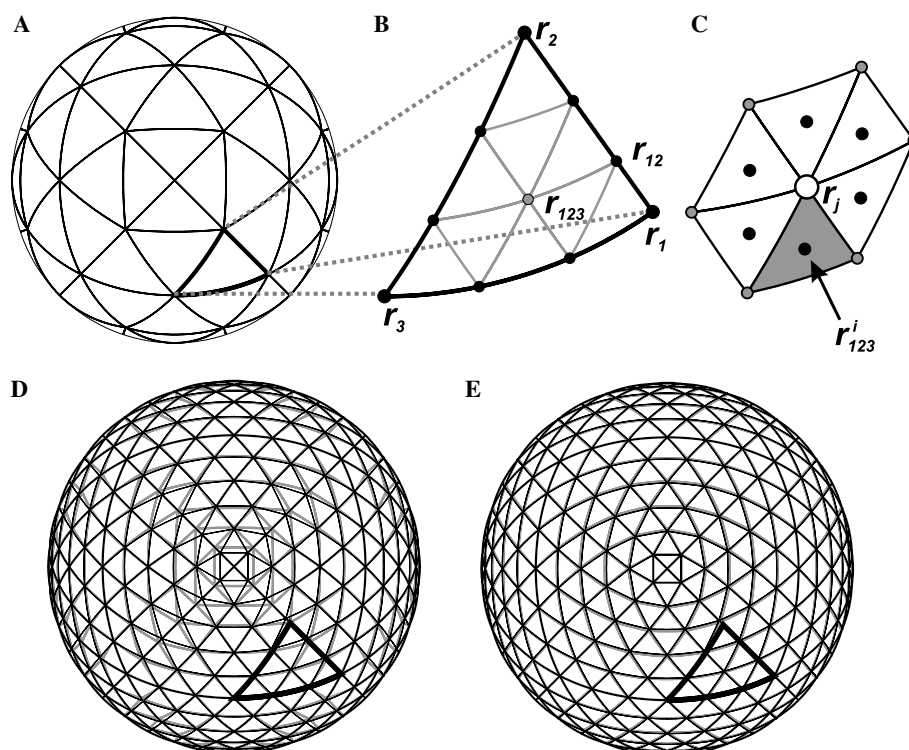

Fig. 2. Illustration of the ROSE procedure. (A) The triangular arrangement of grid points for the (input) LEB50 set. (B) One such triangle, whose vertices are given by the orientations $\mathbf{r}_1$, $\mathbf{r}_2$, and $\mathbf{r}_3$, is used in the octahedral symmetry expansion to construct seven new points: one at the center of the triangle ($\mathbf{r}_{123}$) and three pairs of points on each border. One such point $\mathbf{r}_{12}$ is labeled, and is calculated according to Eq. (25). The octahedral symmetry expansion creates nine new triangles, used subsequently as input to the regularization protocol. (C) Illustration of the six triangles (whose indices are comprised in v_j) sharing a grid point $\mathbf{r}_j$ and used in the regularization procedure. One triangle labelled T_i is shaded, with its center of gravity $\mathbf{r}_{123}^i$ marked. (D) Comparison between the octahedrally symmetry-expanded LEB50 set before (grey lines) and after applying regularization (black lines). The latter is denoted ^{ROSE}LEB434. (E) Comparison between the ^{ROSE}LEB434 set (black lines) and the original "exact" LEB434 set (grey lines).

Table 1
The number of orientations N^S of some representative ^{ROSE}LEB grids: the first column displays the size of the corresponding input LEB grid, with its associated J_{max} given within parenthesis

$N^S_{LEB}(J_{max})$	J^{eff}_{max}	$N^S(^{ROSE}LEB)$	$N^S(^{ROSE}LEBh)$	$N^S(^{ROSE}LEBo)$
770(47)	143	6914	3457	901
974(53)	161	8750	4375	1135
1202(59)	179	10802	5401	1396
1454(65)	197	13070	6535	1684
2030(77)	233	18254	9127	2341
3074(95)	287	27650	13825	3529
4334(113)	341	38990	19495	4960
5810(131)	395	52274	26137	6634

The second column lists the J^{eff}_{max} of the expanded sets. The corresponding number of orientations of the full sphere, hemisphere and octant sets are given in the third, fourth, and fifth columns, respectively.

est-neighboring orientations constitute the vertices of one triangle. One such *set* of triangles is illustrated in Fig. 2A for the LEB50 grid. In the following, an orientation $\{\alpha, \beta\}$ is expressed in the form [43]

$$\mathbf{r}^T = (r_x, r_y, r_z) = (\sin\beta\cos\alpha, \sin\beta\sin\alpha, \cos\beta), \quad (24)$$

where $\mathbf{r}$ is a column vector and T represents the transpose operation.

The next step is to estimate the positions of additional grid points. At the moment, we focus on *one* triangle, depicted in Fig. 2B and defined by the three orientations $\mathbf{r}_1$, $\mathbf{r}_2$, and $\mathbf{r}_3$. This is now triangulated further, by constructing six new points located on its borders, as marked in Fig. 2B. One such point $\mathbf{r}_{12}$ is determined from $\mathbf{r}_1$ and $\mathbf{r}_2$ using the relationships:

$$\mathbf{r}_{12} = \mathbf{r}_1 \cos\{\theta/3\} + (\mathbf{r}_\perp/\|\mathbf{r}_\perp\|)\sin\{\theta/3\}, \quad (25)$$

$$\theta = \arccos\{\mathbf{r}_1^T\mathbf{r}_2\}, \quad (26)$$

$$\mathbf{r}_\perp = \mathbf{r}_2 - \mathbf{r}_1\cos\theta. \quad (27)$$

Here $\mathbf{r}_\perp$ is a vector perpendicular to $\mathbf{r}_1$ and pointing towards $\mathbf{r}_2$, and the length of a vector is calculated as $\|\mathbf{r}\| = \sqrt{\mathbf{r}^T\mathbf{r}}$. The remaining five points on the triangle borders are constructed analogously by permuting the set of vectors $\mathbf{r}_1$, $\mathbf{r}_2$, and $\mathbf{r}_3$. The center-point $\mathbf{r}_{123}$ of the triangle (see Fig. 2B) is calculated as the normalized average of its three surrounding corner points according to

$$\mathbf{r}_{123} = (\mathbf{r}_1 + \mathbf{r}_2 + \mathbf{r}_3)/\|\mathbf{r}_1 + \mathbf{r}_2 + \mathbf{r}_3\|. \quad (28)$$

The procedure outlined above is repeated for *all* triangles, resulting in a grid comprising 434 orientations. It is illustrated by grey lines in Fig. 2D. Starting from an input Lebedev set comprising N orientations, the octahedral symmetry expansion inserts $8(N-2)$ additional grid points and results in an expanded set involving $(9N-16)$ orientations.

3.2. Regularization

A refined set of orientations is achieved by *regularizing* the octahedral symmetry-expanded grid. Our regulariza-

tion is defined on the unit sphere surface and is completed when each orientation is located at the center of gravity of the area spanned by its nearest neighboring grid points. Iterative regularization procedures are discussed further in Ref. [49].

As the regularization operates on a *triangulated* grid of orientations, it is consequently expressed as a set of triangles $\{T_i\}$, where T_i is defined by its three vertices (orientations) $\mathbf{r}_1^i$, $\mathbf{r}_2^i$, and $\mathbf{r}_3^i$. One such triangle is shaded in Fig. 2C. $\mathbf{r}_{123}^i$ represents its center of gravity (calculated by inserting $\mathbf{r}_1^i$, $\mathbf{r}_2^i$, and $\mathbf{r}_3^i$ into Eq. (28)), whereas the triangle area A_{123}^i is given by [50]

$$A_{123}^i = 2\arctan\left\{\frac{|(\mathbf{r}_1^i)^T(\mathbf{r}_2^i \times \mathbf{r}_3^i)|}{1 + (\mathbf{r}_1^i)^T\mathbf{r}_2^i + (\mathbf{r}_1^i)^T\mathbf{r}_3^i + (\mathbf{r}_2^i)^T\mathbf{r}_3^i}\right\}. \quad (29)$$

The absolute value in the numerator accounts for permutations of the vertices and $\mathbf{r}_2^i \times \mathbf{r}_3^i$ represents the cross-product between the vectors $\mathbf{r}_2^i$ and $\mathbf{r}_3^i$.

Next, we introduce a set $\{v_j\}$, where the element v_j comprises a list of all *triangle indices* having $\mathbf{r}_j$ as *vertex*. There are either four or six such triangles sharing an orientation. Fig. 2C shows one such constellation where the point $\mathbf{r}_j$ is surrounded by six triangles. A *refined* orientation $\mathbf{r}_j^{reg}$ is now determined as the weighted sum over its neighboring triangle center-points $\mathbf{r}_{123}^i$ and areas A_{123}^i:

$$\mathbf{r}_j^{reg} = \sum_{i \in v_j} \mathbf{r}_{123}^i A_{123}^i. \quad (30)$$

This procedure is repeated for *all* grid points $\mathbf{r}_j^{reg}$, after which each orientation $\mathbf{r}_j$ is updated as the normalized vector

$$\mathbf{r}_j = \frac{\mathbf{r}_j^{reg}}{\|\mathbf{r}_j^{reg}\|}, \quad (31)$$

leading to a refined set $\{\mathbf{r}_j\}$. The iterative procedure is repeated until convergence is reached, i.e., when all orientations $\mathbf{r}_j$ remain stationary.

Finally, estimates of the positive and essentially equal weights $\{w_j\}$ are obtained posteriori from the fractional area (solid angle) associated with each orientation $\mathbf{r}_j \equiv \{\alpha_j, \beta_j\}$ according to

$$w_j = \mathcal{N}^{(2)}\frac{1}{3}\sum_{i \in v_j} A_{123}^i, \quad (32)$$

where $\mathcal{N}^{(2)}$ is given by Eq. (10) and the factor 1/3 takes into account that the area A_{123}^i is shared equally amongst the vertices of T_i.

Fig. 2E shows a comparison between the existing LEB434 grid and the set of 434 orientations obtained by feeding LEB50 through the ROSE procedure. The differences between LEB434 and ^{ROSE}LEB434 are almost not discernible by eye. The improvement of the regularization step alone is illustrated in (D). It follows that the ROSE approach may be used to predict nearly optimal sets of orientations for cases where the *exact* Lebedev solutions are *not yet existing*. For instance, the currently largest Lebedev

grid ($J_{max} = 131$) gives rise to a ^{ROSE}LEB52274 set with $J_{max}^{eff} = 395$. However, a second application of ROSE results in a grid of 470450 orientations ($J_{max}^{eff} = 1187$).

4. Orientational averaging performance: satellite transitions under MAS

The superiority of the Lebedev scheme compared to other orientational averaging approaches was demonstrated for the calculation of spinning sideband manifolds from dynamically inhomogeneous Hamiltonians [35] in the context of chemical shift anisotropies in powdered samples under MAS conditions [10]. However, in cases of substantial anisotropic interactions, even the largest existing Lebedev sets may be insufficient. It is then necessary to employ the ^{ROSE}LEB schemes. In this section, we compare their performance with other orientational averaging methods for simulating the spinning sideband manifolds generated by the satellite-transitions of a single spin-3/2 in a powder subjected to MAS. The result is a spectrum comprising a set of narrow sidebands, with the sideband envelope width and shape reflecting the size of the quadrupolar frequency ω_Q and the asymmetry parameter η, respectively. Here

$$\omega_Q/2\pi = \frac{3C_Q}{2I(2I-1)}, \tag{33}$$

where $C_Q = e^2qQ/h$ is the quadrupolar coupling constant [36] and I denotes the spin quantum number.

The number of spinning sidebands of significant amplitude increases as the ratio ω_Q/ω_r increases—the higher the ratio, the larger the number of sampled orientations required to reach a converged "powder spectrum." The value of the asymmetry parameter also dictates the convergence properties of a given orientational averaging scheme, as exemplified below. As the number of significant sideband amplitudes only depends on the ratio ω_Q/ω_r, we have employed relatively small quadrupolar frequencies (around $100 - 160$ kHz) in our examples, to ensure that second order quadrupolar interactions [36] are negligible at high magnetic fields and therefore may be omitted in the simulations. Calculations involving second-order broadening are presented in the next section.

As we deal with a single interaction, orientational averaging is sufficient by sampling orientations over an octant. From a set of N^S orientations and weights of a given scheme, we calculated the resulting sideband manifold $\{a_S^{(k)}\}$. The accuracy of the calculated spectrum was assessed by recording the maximum deviation in any amplitude $a_S^{(k)}$ (scanned over all sideband indices k) from the corresponding one $a_{ref}^{(k)}$ in a converged "reference spectrum" [10]:

$$\epsilon_{max}^S = \max_k\{|a_S^{(k)} - a_{ref}^{(k)}|\}. \tag{34}$$

The plot of ϵ_{max}^S against N^S for a given method reflects its orientational averaging performance and will be referred to as its "convergence curve."

We evaluated convergence curves for the LEB sets, in conjunction with its ROSE-expanded versions: throughout, we employ the original octant Lebedev sets out to their currently largest grid-size of 760 ($J_{max} = 131$) and then pursue with the expanded ^{ROSE}LEBo sets. For simplicity, the "combined" convergence curve involving both the Lebedev and ^{ROSE}LEB sets will be referred to as "LEBo": we will comment the onset of the ^{ROSE}LEBo sets whenever needed. The convergence curves of LEBo are compared with those obtained from the octant ASGo [1] and ZCWo [19–21] schemes. These methods were selected as they have proven to be very efficient for powder averaging in NMR [7,10,14], and because arbitrarily large sets of orientations may easily be generated. We have also included results using the full-sphere ZCW sets, as in *some* cases they outperform their octant counterparts.

Fig. 3 depicts the resulting convergence curves (left panel) and the corresponding reference stick spectra (right panel). Fig. 3A shows the case $\omega_Q/2\pi = 100$ kHz, $\eta = 0.3$ and $\omega_r/2\pi = 10$ kHz ($\omega_Q/\omega_r = 10$). For this regime of relatively low ω_Q/ω_r, reflected in a spectrum having 25 sidebands of significant intensity, the Lebedev scheme significantly outperforms all other methods. The dashed line in the left panel indicates an error threshold value below which no visual differences are discernible between the "essentially converged" spectrum and the reference in the right panel of Fig. 3. Here, as well as for other cases discussed below, this amounts to an integration error of 0.5% of the largest spinning sideband amplitude of the manifold. The LEBo scheme reaches well below the threshold in 46 orientations and an *exact* orientational average is obtained using 136 angles. ASG is the second best technique, but requires 1.7 times as many orientations to reach the threshold and 496 crystallites to reduce the error below 10% of the threshold value.

Fig. 3B shows the corresponding curves for the same ω_Q/ω_r ratio but for $\eta = 1.0$. Here as well, the ZCW methods are outperformed by the ASGo and LEBo schemes. LEBo converges well within 64 orientations, while 120 ASGo angles are needed to achieve the same integration accuracy. We have not yet encountered a case where any other tested scheme outperforms the Lebedev method. Additionally, LEB has the advantage of providing *exact* orientational averages.

Fig. 3C displays convergence result for $\omega_Q/\omega_r = 24$ and $\eta = 0.5$, resulting in a larger number of sidebands (~ 60). Here, all schemes consequently require larger sets to converge, but LEBo still performs better than the others. By comparing the two ZCW schemes in (A–C), the very irregular performance of the ZCWo sets are obvious.

Finally, the results of a very challenging case are shown in (D). Here $\omega_Q/2\pi = 162.5$ kHz, $\eta = 0.2$ and $\omega_r/2\pi = 2.5$ kHz, amounting to $\omega_Q/\omega_r = 65$ and giving a sideband manifold comprising ~ 140 sidebands. Now all methods require more than 500 orientations to reach a region of near-convergence, and while the Lebedev scheme reaches this region somewhat faster than the
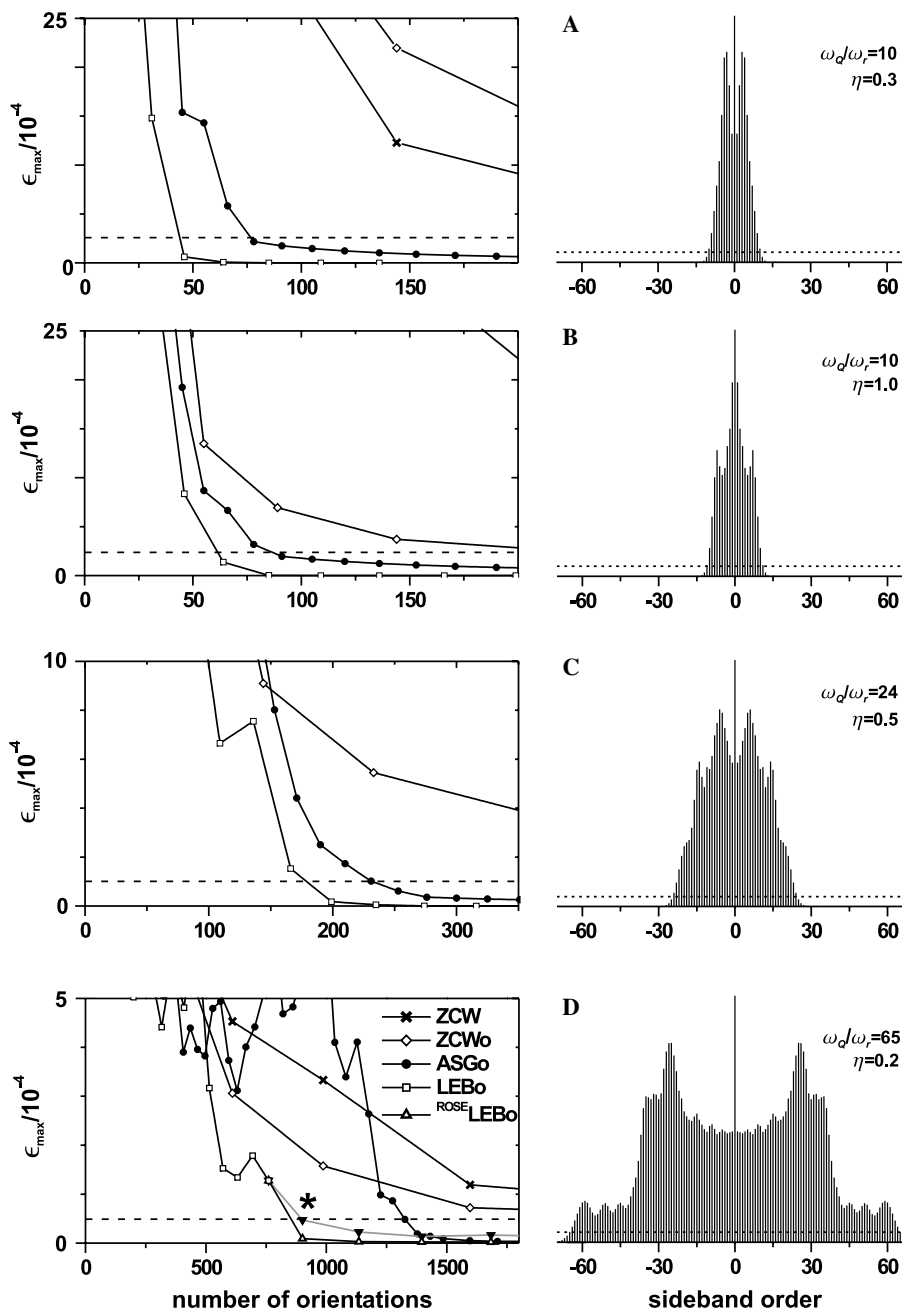
Fig. 3. Powder averaging convergence curves for MAS spectral sideband amplitudes generated by the first-order quadrupolar interaction of a single $I = 3/2$, using parameters as indicated in the right panel of (A–D), also showing the sideband amplitudes of the fully converged reference calculations. The convergence curves of the various sampling schemes compared are identified by the legend in (D). Each dashed line in the *right* panel (at 5% of the maximum sideband amplitude) indicates the maximum value of the vertical scale used in the corresponding convergence plot in the left panel. The central peak whose amplitude mainly derives from the central-transition is truncated for easier visualization. The dashed lines in the *left* panel display an orientational averaging "convergence threshold," as discussed in the text. The asterisk in (D) marks the onset of the octahedrally symmetry-expanded Lebedev sets, *before* (grey line; filled triangles) and *after* applying *regularization* (black line; open triangles).

others, significant competition is provided by ZCWo. Further, the largest existing Lebedev set (760 orientations) fails to reach the convergence threshold and the complementary ^{ROSE}LEB sets now become useful. The curve then forks into two separate paths, one obtained by using the octahedral symmetry expansion *alone* (grey line; filled triangles) and the other resulting after also applying *regularization*, i.e., the ^{ROSE}LEB sets (black line; open triangles). The

marked improvement by using regularization is obvious, and the ^{ROSE}LEB scheme has converged using 901 orientations, which is faster than any other method. As discussed above, the ^{ROSE}LEB sets do not provide exact orientational averages, but the errors introduced are in practice insignificant. This is evident from Fig. 3D, as the integration errors generated by the ^{ROSE}LEB sets consistently stay well below the threshold value (upon convergence).

5. $^{\text{ROSE}}$LEB grids combined with interpolation

The group of orientational averaging problems for which *both* the spectral amplitudes and frequencies are orientation dependent result in broad peakshapes, which may span up to ~1 kHz in the case of homonuclear dipolar-coupling broadened peaks at rotational resonance [45,46], and from tens to hundreds of kHz in cases of substantial anisotropies in static samples. For these calculations, it is necessary to use very large sets of orientations ($10^3 \lesssim N^S \lesssim 10^5$) to avoid simulation artifacts showing up as "rippled" lineshapes (e.g., see Fig. 9 of Ref. [18]). However, the use of spectral interpolation techniques may greatly reduce the number of sampled orientations, while the interpolation procedure itself increases the computation time marginally, in our implementations typically by <10%.

Here we employ the ASG interpolation scheme [1], which requires "triangulated" grids of orientations, i.e., that each grid point may be associated with two neighboring orientations, together making the vertices of a triangle. Naturally, each point is shared between several triangles. The details of the procedure is outlined in [1]. For successful implementation, the ASG interpolation protocol requires that the spin Hamiltonian eigenvalues and eigenvectors associated with each transition are readily distinguished and ordered identically for each triplet of angles employed. This is straightforward for the calculations considered here, for which the spin Hamiltonian is *diagonal*. However, as discussed in Refs. [1,17], some complications arise when dealing with time-dependent non-diagonal Hamiltonians. The ASG interpolation may in principle be adapted to these problems, but we have not pursued such investigations.

The "triangulation" of the Lebedev sets discussed earlier in the context of the ROSE protocol implies that they are suitable for combination with ASG interpolation. As the ROSE procedure itself builds on a triangulation process, the $^{\text{ROSE}}$LEB sets are also well-adapted. However, we have not found any obvious approach to interpolate the ZCW sets.

To assess the performance of the interpolated $^{\text{ROSE}}$LEB schemes, we calculated a set of NMR spectra generated from a spin-3/2 in a powder, in this case including both first and second order quadrupolar interactions. We compared convergence curves obtained from (non-interpolated) ZCW schemes with those of interpolated ASGh and $^{\text{ROSE}}$LEBh sets as follows (for the latter using LEBh sets whenever possible): first, a particular molecular frame M was selected, where Ω_{PM} represents the transformation angles between the PAS of the quadrupolar tensor and M [see Eq. (5)]. Then for a given set S of orientations $\{\Omega^S_{\text{MR}}\}$, we evaluated its powder spectrum and calculated the rms-deviation from a converged reference spectrum, which itself by definition is independent of Ω_{PM}, as follows:

$$\epsilon^S_{\text{rms}}(\Omega_{\text{PM}}) = \left(\frac{1}{n} \sum_{j=1}^{n} \left[a^j_S(\Omega_{\text{PM}}) - a^j_{\text{ref}} \right]^2 \right)^{1/2}. \tag{35}$$

Here $a^j_S(\Omega_{\text{PM}})$ and a^j_{ref} correspond to the jth spectral amplitude obtained using set S and the reference set of orientations, respectively, while n is the total number of amplitudes. Fifty such calculations were repeated, only varying the Ω_{PM} angles (selected from the three-angle ZCW50 set of Ref. [21]) while keeping all other simulation parameters constant. A merit of figure of the accuracy of the orientational average obtained from the set S was extracted as the largest rms-value of the set $\{\epsilon^S_{\text{rms}}(\Omega_{\text{PM}})\}$:

$$\epsilon^S_{\text{max}} = \max_{\Omega_{\text{PM}}} \{\epsilon^S_{\text{rms}}(\Omega_{\text{PM}})\}. \tag{36}$$

The plot of ϵ^S_{max} versus an increasing number of orientations defines the "convergence curve" of the corresponding orientational averaging scheme. This procedure requires using hemispheric sets and was chosen to emulate cases where several non-coincident quadrupolar tensors may be present, thereby precluding the choice $\Omega_{\text{PM}} = \{0, 0, 0\}$. Such a convergence test therefore reflects the "worst-case" orientational averaging performance of a given sampling scheme.

The resulting convergence curves are depicted in the left panel of Fig. 4 for the cases of $C_Q/2\pi$ being equal to (A) 1.0 MHz, (B) 2.5 MHz and (C and D) 4.0 MHz with the Larmor frequency set to $\omega_0/2\pi = -105.9$ MHz. A spinning frequency of 50 kHz was used in (A–C), in order to emulate the case of infinite spinning and ensuring that all signal intensity is present in the central-transition centerband. On the other hand, Fig. 4D employed a spinning speed of 9.0 kHz to test an experimentally more realistic case when spinning sidebands of both first and second order quadrupolar interactions overlap with the centerband (see the inset spectrum). The vertical scale of each convergence plot is set so as to illustrate "poor" and "decent" orientational averaging convergence around the top and bottom portions of each figure, respectively. The right panel shows the reference spectra, together with error functions representing the deviations between the reference spectrum and that obtained from a particular set of orientations.

Here, Fig. 4 reveals no significant differences between the two interpolated schemes: $^{\text{ROSE}}$LEBh is slightly better than ASGh and converges roughly 15–20% faster. For all cases, decent "convergence" is achieved in ~7000 orientations, despite that the quadrupolar coupling increases in (A–C) and thereby result in increasingly broadened peakshapes. The similar convergence is due to the application of Gaussian broadening amounting to $\lesssim 1\%$ of the *central-transition peak-width* in *each* case. Increasing the broadening further leads to faster convergence for all methods, and particularly so for the non-interpolated schemes, while the relative convergence of ASG and $^{\text{ROSE}}$LEB remain essentially unchanged. Our choice of a relatively small broadening was for the sake of emphasizing the different orientational averaging performance of the sampling schemes, as well as on the impact of using interpolation. It should be noted that use of extensive additional
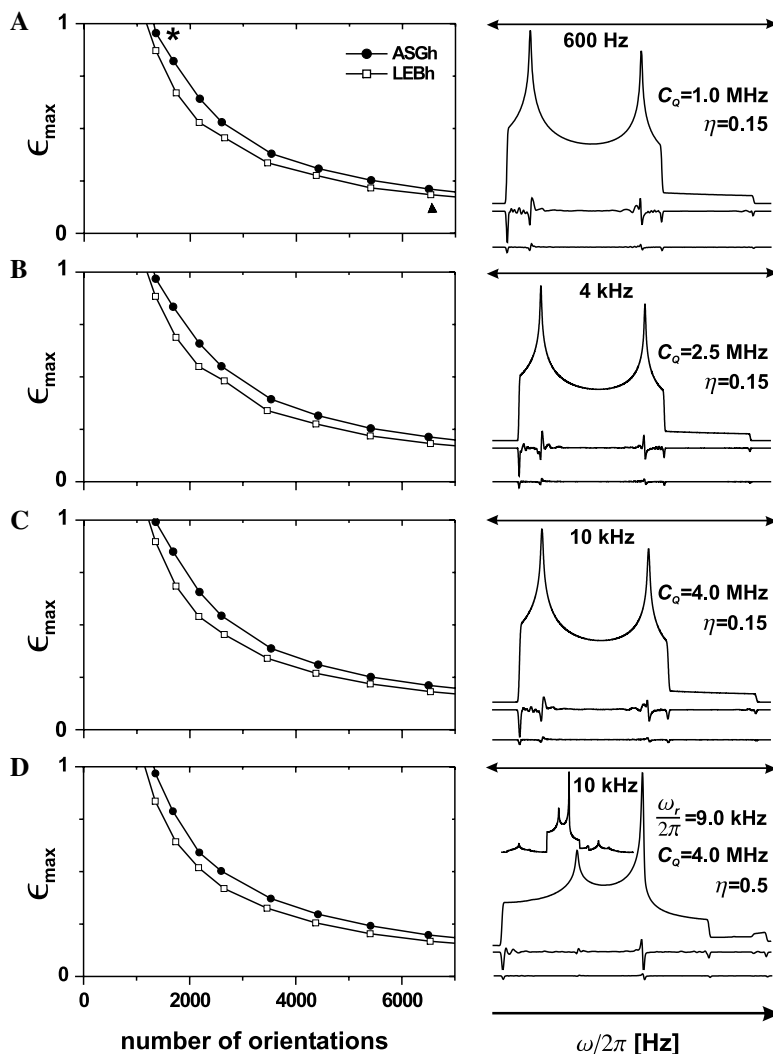
Fig. 4. Powder averaging convergence curves for the two interpolated hemispheric schemes ASGh and LEBh; the latter represent Lebedev orientations up to the grid-size 2647, after which the expanded ^{ROSE}LEBh sets are employed. These test cases involve second-order quadrupolar broadened central transition peakshapes of spins—3/2, assuming a Larmor frequency $\omega_0/2\pi = -105.9$ MHz, which is representative for ^{23}Na at 9.4 T. The calculations employed parameters as indicated in each plot, using a MAS frequency of 50 kHz in (A–C). In (D), both central and satellite transitions were detected. In this case of a moderate spinning frequency (9 kHz) the sidebands of both the satellite and central transitions overlap (see inset in (D)). Difference ("error") spectra are shown beneath each reference spectrum in the right panel. They were obtained using either the ASGh1353 set (marked by asterisk in (A)) and the ^{ROSE}LEBh6535 set (triangle), and indicate the level of convergence around the upper and lower regions of each plot in the left panel, whose maximum values of the vertical scale are arbitrarily set to 1.

broadening amounts to a similar effect as spectral interpolation, but also *alters* spectral features, as the sharp singularities of the lineshapes are "smeared" out.

The convergence properties are displayed further in Fig. 5, where $\log_{10}\{\epsilon^S_{max}\}$ is plotted against $\log_{10}\{N^S\}$. Vast differences between interpolated and non-interpolated techniques are (not surprisingly) observed. Employing interpolation for this type of problems makes substantial differences [1,17], and whereas the ^{ROSE}LEB scheme converges slightly faster than ASG, the main simulation accelerator is the use of interpolation alone. We also mention that similar calculations (not shown) using $\Omega_{PM} = \{0,0,0\}$, thereby permitting averaging over an octant, generally favored ^{ROSE}LEBo, amounting to 25–30% faster convergence compared to ASGo.

Our tests focussed on simulations of powder patterns from fourth-rank tensors in the case of spins—3/2 under MAS conditions [36]. However, these results are representative for spectral calculations of any half-integer quadrupolar spin under MAS, and likely also to cases where both second- and fourth-rank tensors contribute (e.g., quadrupolar spins in static powders) as well as to scenarios where only second-rank tensors are involved, e.g., chemical shift anisotropies and heteronuclear dipolar couplings in static samples.

6. Numerical procedures

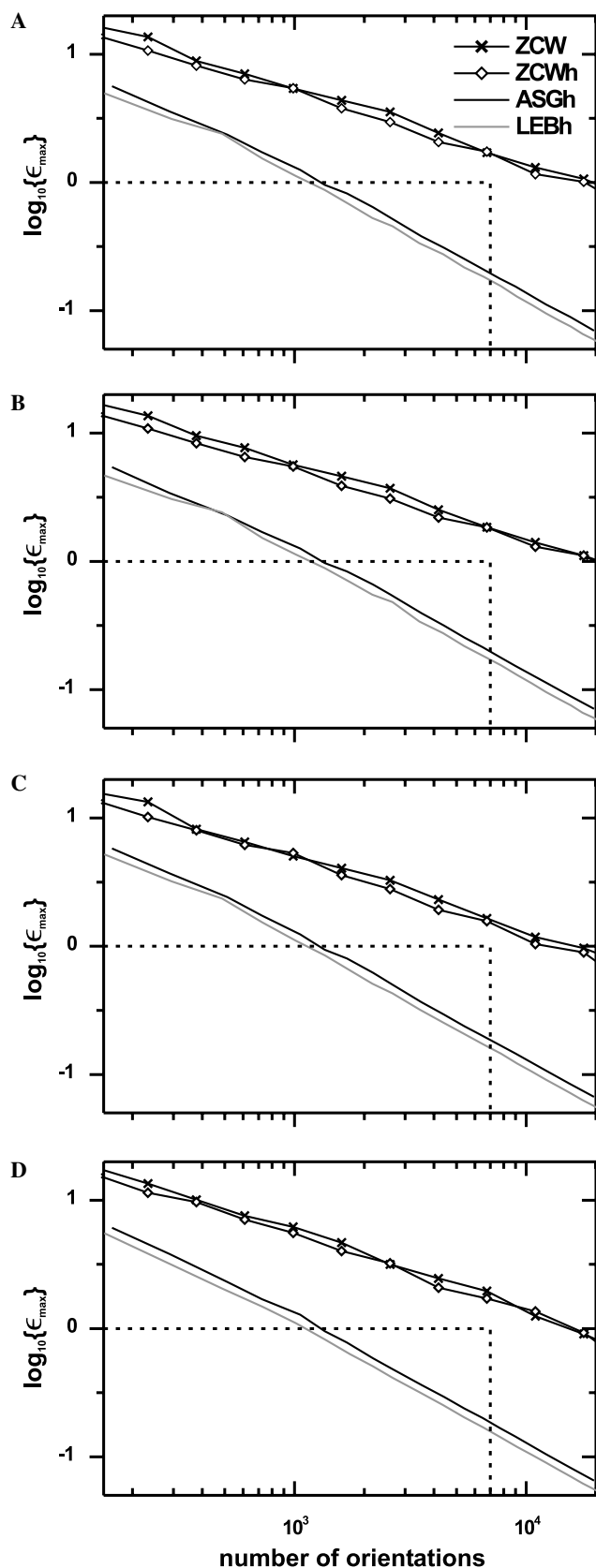All spectral simulations were based on the COMPUTE protocol [48], with the integration over γ handled separate-

ly using the methods in [11,12]. By dividing the rotational period into a large number of segments n [48], we ensured that negligible errors were introduced from the time integration of the Schrödinger equation. For example, in the spinning sideband calculations of Fig. 3, n ranged between 256 and 2048. The simulations in Fig. 3 included only first order quadrupolar interactions, whereas those in Figs. 4 and 5 incorporated both first and second order quadrupolar interactions. For the latter, the spectral amplitudes output from the COMPUTE calculation were sorted into bins as discussed in detail in Ref. [51]. In Fig. 4, additional Gaussian broadening of (A) 3.5 Hz, (B) 17 Hz and (C and D) 70 Hz were employed, with the broadening always exceeding the spectral resolution by at least an order of magnitude. All cases used an initial density operator $\widehat{\rho} = \widehat{I}_x$. The detection operator corresponded to $\widehat{I}^+$ in Fig. 4D, whereas only the central-transition was observed in (A–C) using the fictitious spin-1/2 operator $\widehat{I}_{CT}^+$ of the central-transition subspace [52,53].

The error functions displayed in the right panel of Fig. 4 were calculated as the difference between the converged reference spectrum and that obtained using the Euler angle triplet Ω_{PM} giving the maximum error ϵ_{max}^S in Eq. (36), i.e.,

$$\epsilon_S^j = a_S^j(\Omega_{PM}) - a_{ref}^j, \quad j = 1, 2, \ldots n, \tag{37}$$

where j is the amplitude coordinate and n the total number of amplitudes.

"Exact" reference spectra were generated in Fig. 3A–C using the LEBo760 set, whereas 3524578 ZCW orientations were employed in (D) and in Figs. 4 and 5. The rank profile calculations in Fig. 1 incorporated the procedure presented in Appendix A. Only even-rank $D_{q0}^J(\alpha, \beta)$ functions needed to be evaluated for these hemispheric sets [10].

7. Conclusions

The largest existing Lebedev set of orientations [28–33] is insufficient for calculating orientational averages in NMR if the anisotropic interactions are substantial. As exact Lebedev solutions for larger grids cannot easily be found, we have introduced the *r*egularized *o*ctahedral *s*ymmetry *e*xpansion (ROSE) protocol. This recursive procedure is straightforward to implement and generates new near-optimal Lebedev orientations. Each ROSE-step leads to a 9-fold enlargement of the input grid. For all practical purposes, the new ROSELEB sets provide comparable integration accuracies as the "exact" GSQ methods.

The problem of orientational averaging in solid state NMR may broadly be classified as follows: (i) only the NMR spectral amplitudes depend on orientation and (ii) both the amplitudes and frequencies are orientation dependent. In the first case, Lebedev sets in conjunction with their ROSE-expanded counterparts are superior to other orientational averaging methods: to achieve a decent integration accuracy, the second best technique (ASG) typically requires 1.5 times as many orientations. If very high accuracy is required, ROSELEB gives an order of magnitude

Fig. 5. Same simulations as in Fig. 4, but showing log–log convergence plots. The dashed boxes indicate the ranges employed in the plots of Fig. 4. Note the large differences between interpolated (ASGh and LEBh) and non-interpolated (ZCW and ZCWh) methods.

reduced computation time. For the second category of NMR powder simulations, typically very broad lineshapes are obtained. For an important sub-group of these problems, namely when the spin Hamiltonian is *diagonal*, we demonstrated in the context of isolated quadrupolar spins undergoing MAS that [ROSE]LEB sets in conjunction with the interpolation protocol of Alderman, Solum, and Grant gives faster convergence of the powder lineshapes than using the original ASG orientational sampling scheme [1]. However, the gains are rather marginal, typically amounting to 15–25% reduced computation time. We emphasize the benefits of using spectral interpolation [1,17], as the interpolated ASG and [ROSE]LEB schemes are superior to other methods that cannot straightforwardly exploit interpolation, such as ZCW [19–21] or REPULSION [7]. However, currently the ASG interpolation procedure is problematic to implement for cases where the spin Hamiltonian is *non*-diagonal: this applies, for instance, to calculations involving homonuclear couplings. Improved interpolation strategies would be valuable for this group of problems.

In summary, the [ROSE]LEB schemes are very efficiently dealing with broad classes of orientational averaging problems in solid state NMR, and arbitrarily large grids may be obtained by using the expansion recursively. [ROSE]LEB grids together with data for implementing spectral interpolation may be obtained from the authors [54]. These schemes should be helpful to the users of current public NMR simulation platforms, such as GAMMA [39], SIMPSON [17,40], BlochLib [41] and SPINEVOLUTION [42]. Further, the ROSE sets are expected to be beneficial for many other applications where Lebedev sets are exploited, for example in DFT-calculations [22–27].

Acknowledgments

Appendix A

The *real*-valued reduced Wigner function $d_{qq'}^J(\beta)$ may be expressed analytically as [43]

$$d_{qq'}^J(\beta) = [(J+q)!(J-q)!(J+q')!(J-q')!]^{\frac{1}{2}}$$
$$\times \sum_k (-1)^k \frac{(\cos\frac{\beta}{2})^{2J-2k+q-q'}(\sin\frac{\beta}{2})^{2k-q+q'}}{k!(J+q-k)!(J-q'-k)!(q'-q+k)!}. \quad (38)$$

Eq. (38) is straightforward to evaluate, but is prone to accumulating numerical errors, which makes it difficult to implement for high ranks ($J \gtrsim 100$). For the calculations in Fig. 1, we instead employed the procedure outlined below, which appears to be numerically stable and at least as efficient as using Eq. (38).

The reduced Wigner function $d_{qq'}^J(\beta)$ is defined [43]

$$d_{qq'}^J(\beta) \equiv \langle q | \exp\{-i\beta \widehat{J}_y\} | q' \rangle, \quad (39)$$

where $\widehat{J}_y$ is the y-angular momentum operator of a spin-*J*. To avoid intermediate complex numerics of the real-valued function $d_{qq'}^J(\beta)$ (thereby saving computational time and accuracy), we exploit the identity [55]

$$\widehat{J}_y \equiv \exp\left\{-i\frac{\pi}{2}\widehat{J}_z\right\}\widehat{J}_x \exp\left\{i\frac{\pi}{2}\widehat{J}_z\right\}. \quad (40)$$

Using well-known properties of exponential operators [55], the combination of Eqs. (39) and (40) gives

$$d_{qq'}^J(\beta) = \langle q | \exp\left\{-i\frac{\pi}{2}\widehat{J}_z\right\} \exp\{-i\beta\widehat{J}_x\}$$
$$\times \exp\left\{i\frac{\pi}{2}\widehat{J}_z\right\} | q' \rangle. \quad (41)$$

The operator $\widehat{J}_x$ is diagonalized through

$$\widehat{J}_x = \widehat{X}_J \widehat{J}_z \widehat{X}_J^T, \quad (42)$$

where the operator $\widehat{J}_z$ is diagonal, and the columns in the matrix representation of $\widehat{X}_J$ corresponds to the eigenvectors of $\widehat{J}_x$. Since the operators $\widehat{J}_x$ and $\exp\{-i\beta\widehat{J}_x\}$ share the same eigenvectors [56], Eq. (41) may be expressed

$$d_{qq'}^J(\beta) = \sum_{j,k,l,m=-J}^{J} \langle q | \exp\left\{-i\frac{\pi}{2}\widehat{J}_z\right\} | j \rangle \langle j | \widehat{X}_J | k \rangle$$
$$\times \langle k | \exp\{-i\beta\widehat{J}_z\} | l \rangle \langle l | \widehat{X}_J^T | m \rangle$$
$$\times \langle m | \exp\left\{i\frac{\pi}{2}\widehat{J}_z\right\} | q' \rangle. \quad (43)$$

After exploiting that $\widehat{J}_z$ is diagonal, $\langle q | \exp\{-i\beta\widehat{J}_z\} | q' \rangle = \exp\{-i\beta q\}\delta_{q,q'}$ and the property $\langle l | \widehat{X}_J^T | m \rangle = \langle m | \widehat{X}_J | l \rangle$, the sum collapses into $2J+1$ terms:

$$d_{qq'}^J(\beta) = \sum_{k=-J}^{J} \langle q | \exp\left\{-i\frac{\pi}{2}\widehat{J}_z\right\} | q \rangle \langle q' | \exp\left\{i\frac{\pi}{2}\widehat{J}_z\right\} | q' \rangle$$
$$\times \langle k | \exp\left\{-i\beta\widehat{J}_z\right\} | k \rangle \langle q | \widehat{X}_J | k \rangle \langle q' | \widehat{X}_J | k \rangle. \quad (44)$$

Since the reduced Wigner functions are real-valued, this may be simplified further into

$$d_{qq'}^J(\beta) = \sum_{k=-J}^{J} \cos\left\{(q'-q)\frac{\pi}{2} - \beta k\right\} \langle q | \widehat{X}_J | k \rangle \langle q' | \widehat{X}_J | k \rangle. \quad (45)$$

It follows that by using Eq. (45), one may evaluate all $(2J+1)^2$ functions $d_{qq'}^J(\beta)$ through the diagonalization of a real symmetric matrix of dimension $(2J+1)$ [Eq. (42)]. The diagonalization itself is computer-intensive, but needs only be performed *once* if the resulting eigenvectors are stored for future use.

References

[1] D.W. Alderman, M.S. Solum, D.M. Grant, Methods for analyzing spectroscopic line shapes. NMR solid powder patterns, J. Chem. Phys. 84 (1986) 3717–3725.

[2] M.J. Mombourquette, J.A. Weil, Simulation of magnetic resonance powder spectra, J. Magn. Reson. 99 (1992) 37–44.

[3] L. Andreozzi, M. Giordano, D. Leporini, A fast algorithm for magnetic resonance lineshapes of powder samples, J. Magn. Reson. A 104 (1993) 166–171.

[4] J.M. Koons, E. Hughes, H.M. Cho, P.D. Ellis, Extracting multitensor solid-state NMR parameters from lineshapes, J. Magn. Reson. A 114 (1995) 12–23.

[5] D. Wang, G.R. Hanson, A new method for simuling randomly oriented powder spectra in magnetic resonance: the Sydney Opera House (SOPHE) method, J. Magn. Reson. A 117 (1995) 1–8.

[6] S.J. Varner, R.L. Vold, G.L. Hoatson, An efficient method for calculating powder patterns, J. Magn. Reson. A 123 (1996) 72–80.

[7] M. Bak, N.C. Nielsen, REPULSION—a novel approach to efficient powder averaging in solid-state NMR, J. Magn. Reson. 125 (1997) 132–139.

[8] T. Charpentier, C. Fermon, J. Virlet, Efficient time propagation technique for MAS NMR simulation: application to quadrupolar nuclei, J. Magn. Reson. 132 (1998) 181–190.

[9] T. Charpentier, C. Fermon, J. Virlet, Numerical and theoretical analysis of multiquantum magic-angle-spinning experiments, J. Chem. Phys. 109 (1998) 3116–3130.

[10] M. Edén, M.H. Levitt, Computation of orientational averages in solid-state NMR by gaussian spherical quadrature, J. Magn. Reson. 132 (1998) 220–239.

[11] M.H. Levitt, M. Edén, Numerical simulation of periodic NMR problems: fast calculation of carousel averages, Mol. Phys. 95 (1998) 879–890.

[12] M. Hohwy, H. Bildsøe, H.J. Jakobsen, N.C. Nielsen, Efficient spectral simulations in NMR of rotating solids. The γ-COMPUTE algorithm, J. Magn. Reson. 136 (1999) 6–14.

[13] A. Ponti, Simulation of one-dimensional magnetic resonance powder lineshapes reduced to area computation, Chem. Phys. Lett. 302 (1999) 224–230.

[14] A. Ponti, Simulation of magnetic resonance static powder lineshapes: a quantitative assessment of spherical codes, J. Magn. Reson. 138 (1999) 288–297.

[15] P. Hodgkinson, L. Emsley, Numerical simulation of solid-state NMR experiments, Prog. NMR Spectrosc. 36 (2000) 201–239.

[16] M. Mehring, V.A Weberuss, Object-Oriented Magnetic Resonance. Classes and Objects, Calculations and Computations, Academic Press, London, 2001.

[17] T. Vosegaard, A. Malmendal, N.C. Nielsen, The flexibility of SIMPSON and SIMMOL for numerical simulations in solid- and liquid-state NMR spectroscopy, Chem. Monthly 133 (2002) 1555–1574.

[18] M. Edén, Computer simulations in solid state NMR: III. Powder averaging, Concepts Magn. Reson. A 18 (2003) 24–55.

[19] S.K. Zaremba, Good lattice points, discrepancy, and numerical integration, Ann. Mat. Pura. Appl. 4 (73) (1966) 293–317.

[20] H. Conroy, Molecular Schrödinger equation. VIII. A new method for the evaluation of multidimensional integrals, J. Chem. Phys. 47 (1967) 5307–5318.

[21] V.B. Cheng, H.H. Suzukawa, M. Wolfsberg, Investigations of a nonrandom numerical method for multidimensional integration, J. Chem. Phys. 59 (1973) 3992–3999.

[22] C.W. Murray, N.C. Handy, G.J. Laming, Quadrature schemes for integrals of density functional theory, Mol. Phys. 78 (1993) 997–1014.

[23] O. Treutler, R. Ahlrichs, Efficient molecular numerical integration schemes, J. Chem. Phys. 102 (1995) 346–354.

[24] C. Daul, S. Daul, Symmetrical "nonproduct" quadrature rules for a fast calculation of multicenter integrals, Int. J. Quant. Chem. 61 (1997) 219–230.

[25] X.G. Wang, T. Carrington, Using Lebedev grids, sine spherical harmonics, and monomer contracted basis functions to calculate bending energy levels of HF trimer, J. Theor. Comput. Chem. 2 (2003) 599–608.

[26] A. Furuhama, S. Ten-no, Integral equation theory of distributed partial wave bases: application to molecular liquids, Chem. Phys. Lett. 384 (2004) 376–381.

[27] S.T. Brown, L. Füsti-Molnár, J. Kong, Interpolation density values on a cartesian grid: Improving the efficiency of Lebedev based numerical integration in Kohn-Sham density functional algorithms, Chem. Phys. Lett. 418 (2005) 486–491.

[28] V.I. Lebedev, Values of the nodes and weights of ninth to seventeenth order gauss-markov quadrature formulae invariant under the octahedron group with inversion, Zh. Vychisl. Mat. Mat. Fiz. 15 (1975) 48–54.

[29] V.I. Lebedev, Quadratures on a sphere, Zh. Vychisl. Mat. Fiz. 16 (1976) 293–306.

[30] V.I. Lebedev, Spherical quadrature formulas exact to orders 25–29, Sibirsk. Mat. Zh. 18 (1977) 132–142.

[31] V.I. Lebedev, A.L. Skorokhodov, Quadrature formulas of orders 41, 47 and 53 for the sphere, Russian Acad. Sci. Dokl. Math. 45 (1992) 587–592.

[32] V.I. Lebedev, A quadrature formula for the sphere of 59th algebraic order of accuracy, Russian Acad. Sci. Dokl. Math. 50 (1995) 283–286.

[33] V.I. Lebedev, D.N. Laikov, A quadrature formula for the sphere of the 131st algebraic order of accuracy, Dokl. Math. 59 (1999) 477–481.

[34] B. Delley, High order integration schemes on the unit sphere, J. Comp. Chem. 17 (1996) 1152–1155.

[35] M.M. Maricq, J.S. Waugh, NMR in rotating solids, J. Chem. Phys. 70 (1979) 3300–3316.

[36] A. Jerschow, From nuclear structure to the quadrupolar NMR interaction and high-resolution spectroscopy, Prog. NMR Spectrosc. 46 (2005) 63–78.

[37] K.E. Gates, M. Griffin, G.R. Hanson, K. Burrage, Computer simulation of magnetic resonance spectra employing homotropy, J. Magn. Reson. 135 (1998) 104–112.

[38] U. Haeberlen, High Resolution NMR in Solids. Selective Averaging, Academic Press, New York, 1976.

[39] S.A. Smith, T.O. Levante, B.H. Meier, R.R. Ernst, Computer simulations in magnetic resonance. An object-oriented programming approach, J. Magn. Reson. A 106 (1994) 75–105.

[40] M. Bak, J.T. Rasmussen, N.C. Nielsen, SIMPSON: a general simulation program for solid-state NMR spectroscopy, J. Magn. Reson. 147 (2000) 296–330.

[41] W.B. Blanton, BlochLib: a fast NMR C++ tool kit, J. Magn. Reson. 162 (2003) 269–283.

[42] M. Veshtort, R.G. Griffin, SPINEVOLUTION: a powerful tool for the simulation of solid and liquid state NMR experiments, J. Magn. Reson. 178 (2006) 248–282.

[43] D.A Varshalovich, A.N Moskalev, V.K Khersonskii, Quantum Theory of Angular Momentum, World Scientific, Singapore, 1988.

[44] M. Edén, Computer simulations in solid state NMR: I. Spin dynamics theory, Concepts Magn. Reson. A 17 (2003) 117–154.

[45] M.G. Colombo, B.H. Meier, R.R. Ernst, Rotor-driven spin diffusion in natural abundance ¹³C spin systems, Chem. Phys. Lett. 146 (1988) 189–196.

[46] M.H. Levitt, D.P. Raleigh, F. Creuzet, R.G. Griffin, Theory and simulations of homonuclear spin pair systems in rotating solids, J. Chem. Phys. 90 (1990) 6347–6364.

[47] M.H. Levitt, Why do spinning sidebands have the same phase? J. Magn. Reson. 82 (1989) 427–433.

[48] M. Edén, Y.K. Lee, M.H. Levitt, Efficient simulation of periodic problems in NMR. Application to decoupling and rotational resonance, J. Magn. Reson. A 120 (1996) 56–71.

[49] A. Quarteroni, R. Sacco, F. Saleri, Numerical Mathematics, Springer, New York, 2000.

[50] A. van Osterom, J. Strackee, The solid angle of a plane triangle, IEEE Trans. Biomed. Eng. 30 (1983) 125–126.

[51] M. Edén, Computer simulations in solid state NMR: II. Implementations for static and rotating samples, Concepts Magn. Reson. A 18 (2003) 1–23.

[52] A. Wokaun, R.R. Ernst, Selective excitation and detection in multilevel spin systems: application of single transition operators, J. Chem. Phys. 67 (1977) 1752–1758.

[53] S. Vega, Fictitious spin 1/2 operator formalism for multiple quantum NMR, J. Chem. Phys. 68 (1978) 5518–5527.

[54] http://www.fos.su.se/~mattias.

[55] M.H Levitt, Spin Dynamics. Basics of Nuclear Magnetic Resonance, Wiley, Chichester, 2001.

[56] J.J Sakurai, Modern Quantum Mechanics, Addison-Wesley, New York, 1994.